

Shell-ferromagnetism and decomposition in off-stoichiometric $\text{Ni}_{50}\text{Mn}_{50-x}\text{Sb}_x$ Heuslers

Cite as: J. Appl. Phys. **125**, 043902 (2019); <https://doi.org/10.1063/1.5057763>

Submitted: 15 September 2018 . Accepted: 08 January 2019 . Published Online: 30 January 2019

Z. Wanjiku, A. Çakır,  F. Scheibel,  U. Wiedwald,  M. Farle, and  M. Acet



View Online



Export Citation



CrossMark

ARTICLES YOU MAY BE INTERESTED IN

Annealing-time and annealing-temperature dependencies of the size of Ni-Mn-In shell-ferromagnetic nano-precipitates by Scherrer analysis

AIP Advances **8**, 025012 (2018); <https://doi.org/10.1063/1.5018851>

Shell-ferromagnetism in a Ni-Mn-In off-stoichiometric Heusler studied by ferromagnetic resonance

AIP Advances **7**, 056425 (2017); <https://doi.org/10.1063/1.4976335>

Shell-ferromagnetism in Ni-Mn-based Heuslers in view of ductile Ni-Mn-Al

AIP Advances **7**, 056424 (2017); <https://doi.org/10.1063/1.4975792>



Your Qubits. Measured.

Meet the next generation of quantum analyzers

- Readout for up to 64 qubits
- Operation at up to 8.5 GHz, mixer-calibration-free
- Signal optimization with minimal latency

Find out more



Shell-ferromagnetism and decomposition in off-stoichiometric $\text{Ni}_{50}\text{Mn}_{50-x}\text{Sb}_x$ Heuslers

Cite as: J. Appl. Phys. **125**, 043902 (2019); doi: [10.1063/1.5057763](https://doi.org/10.1063/1.5057763)

Submitted: 15 September 2018 · Accepted: 8 January 2019 ·

Published Online: 30 January 2019







View Online



Export Citation



CrossMark

Z. Wanjiku,^{1,2} A. Çakır,^{1,3} F. Scheibel,^{1,4}  U. Wiedwald,¹  M. Farle,¹  and M. Acet^{1,a)} 

AFFILIATIONS

¹Faculty of Physics, University of Duisburg-Essen, 47057 Duisburg, Germany

²Department of Physical Sciences, Chuka University, P.O. Box 109, 60400 Chuka, Kenya

³Department of Metallurgical and Materials Engineering, Muğla Sıtkı Koçman University, 48000 Mugla, Turkey

⁴Materials Science (Materialwissenschaft), Technische Universität, 64287 Darmstadt, Germany

a) mehmet.acet@uni-due.de

ABSTRACT

Off stoichiometric Heuslers in the form $\text{Ni}_{50}\text{Mn}_{50-x}\text{Z}_x$, where Z can be a group 13–15 element of the periodic system, decompose at about 650 K into a ferromagnetic full Heusler $\text{Ni}_{50}\text{Mn}_{25}\text{Z}_{25}$ and an antiferromagnetic $\text{Ni}_{50}\text{Mn}_{50}$ component. We study here the case for Z as Sb and report on shell-ferromagnetic properties as well as thermal instabilities. Unlike the case for other Z-elements, in $\text{Ni}_{50}\text{Mn}_{50-x}\text{Sb}_x$, the minimum decomposition temperature corresponds to a temperature lying within the austenite state so that it is possible to observe the change in the martensitic transition temperature while annealing, thus providing further information on the change of composition during annealing. Scherrer analysis performed on emerging peaks related to the cubic full-Heusler shows that the precipitate size for shell-FM properties to become observable is around 5–10 nm. Other than vertical shifts in the field-dependence of the magnetization, which are also observed in compounds with Z other than Sb, concurrent exchange-bias effects are observed in the case with Z as Sb.

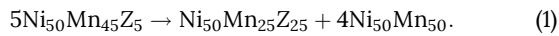
© 2019 Author(s). All article content, except where otherwise noted, is licensed under a Creative Commons Attribution (CC BY) license (<http://creativecommons.org/licenses/by/4.0/>). <https://doi.org/10.1063/1.5057763>

I. INTRODUCTION

Heusler alloys have many functionalities based on the presence of first order magnetostructural transitions. These appear particularly in Ni-Mn-based Heuslers with composition $\text{Ni}_{50}\text{Mn}_{50-x}\text{Z}_x$ where Z can be Al, Ga, In, Sn, and Sb.¹ They have potential room-temperature applications in the areas of magnetic shape-memory,^{2,3} magnetocalorics,^{4,5} and giant magnetoresistance.⁶ These alloys are not only interesting for their functionalities, but they also serve as prototypes for investigating basic physical phenomena such as solid-solid phase transitions,⁷ kinetic arrest,^{8,9} and intrinsic exchange bias,^{10–12} most of which are related to the presence of mixed magnetic interactions at the microscopic scale. Just how these interactions relate to the multifunctional properties in the macroscopic scale is a topic of current research.

Another recently discovered property of these off-stoichiometric alloys that is less known and less studied is the shell-ferromagnetic effect. Off stoichiometric Ni-Mn-based Heusler alloys in the form $\text{Ni}_{50}\text{Mn}_{50-x}\text{Z}_x$ (Z: Al, Ga, In, Sn, Sb) decompose into cubic $L2_1$ ferromagnetic (FM) Heusler $\text{Ni}_{50}\text{Mn}_{25}\text{Z}_{25}$ and $L1_0$ antiferromagnetic (AF) $\text{Ni}_{50}\text{Mn}_{50}$ components when annealed in the temperature-range $600 \leq T_a \leq 750$ K, where T_a is the annealing temperature.^{13–18} In the case $x = 5$, the shell-FM effect is observed when the annealing takes place in a magnetic field: The compound decomposes into a FM Heusler component as 2–5 nm precipitates, while the surrounding matrix component becomes AF with a large magnetocrystalline anisotropy.^{19,20} The moments of the shell of the FM precipitate become pinned in the direction of the annealing field so that the field-dependence up to 9 T appears as a vertically shifted hysteresis loop,

whereas it is actually a minor loop within a major loop with a coercive field of 10–20 T. The remanent magnetizations of the loops are always positive.^{22–24} The interior of the precipitate is, however, magnetically soft, and the spins rotate freely in the direction of an applied magnetic field. For all compositions, the decomposition reaction can be described as



A permanent shell-FM alignment is thermally stable up to 550 K and is unaffected by high magnetic fields up to 9 T. They were first found in the Ni-Mn-In series as a result of decomposing $\text{Ni}_{50}\text{Mn}_{45}\text{In}_5$ at 650 K in a magnetic field. The shell-FM effect is observable when the surface-to-volume ratio of the precipitates is sufficiently large. If the precipitate is too large, the surface-to-volume ratio becomes small, and the shell-FM effect is masked by the volume magnetization of the precipitates. The size of the precipitates formed by annealing $\text{Ni}_{50}\text{Mn}_{45}\text{In}_5$ at 650 K has recently been determined by Scherrer analysis to be in the order of 2–5 nm corresponding to a surface-to-volume ratio of 1.5–0.6 nm⁻¹.²⁵

In this work, we turn our attention to the $\text{Ni}_{50}\text{Mn}_{50-x}\text{Sb}_x$ series which has been extensively studied for their multi-functional properties.^{26–33} Here, we introduce and study the shell-FM properties and, in addition, the thermal instabilities in the compositional range $5.4 \leq x \leq 15.3$ at. % (hereafter, the unit at. % will be dropped). We further study the development of the size of the precipitates in $x = 5.4$ as a function of annealing temperature T_a and annealing time t_a . For Z as Sb, the compositional dependence of the characteristic martensitic transition temperatures is more rapid than for other Z-elements so that for $x = 5.4$, annealing at $T_a \geq 650$ K occurs in the austenite state rather than in the martensite state as in the other Z-elements with similar composition. Therefore, it should be possible to observe any shift in the martensitic transition temperature due to changes in the composition while annealing progresses and the shell-FM precipitates generate. The amount of shift should also give an idea of how the composition itself varies over various time scales. Furthermore, the dependence of the Curie temperature of the austenite state on the valence-electron-concentration for Z as Sb runs at higher values than in the case when Z is other than Sb.³⁰ This could cause the Heusler precipitate $\text{Ni}_{50}\text{Mn}_{25}\text{Sb}_{25}$ to have a stronger FM exchange than in the other Heusler counterparts and lead to even more enhanced shell-FM pinning.

Since magnetostructural transitions in $\text{Ni}_{50}\text{Mn}_{50-x}\text{Sb}_x$ Heusler-based alloys, in particular at off-stoichiometric compositions, are exploited for possible applications, it is important to understand their compositional stability after subjecting them to various heat treatments. This and the case when heat treatments take place in the presence of a magnetic field and lead to the shell-FM effect are studied in the present paper.

II. EXPERIMENT

$\text{Ni}_{50}\text{Mn}_{50-x}\text{Sb}_x$ polycrystalline samples with $x = 5.4, 10.1, 12.5,$ and 15.3 were prepared by arc melting of high purity elements (99.99%) and were annealed under Ar at 1073 K in sealed quartz tubes for 5 days. They were then quenched in water at room temperature. The compositions of the initial samples were determined with energy dispersive x-ray (EDX) analysis using a scanning electron microscope. To check for the sample homogeneity, EDX spectra were collected from three different areas. The deviations in the compositions were no more than 0.05% for all elements. The compositions of the four samples are listed in Table I.

The ingots were ground to powder and re-annealed at 1073 K for 1 day to remove residual strains. About 30 mg powder-samples were used first in the in-field decomposition and magnetization studies. Temperature- and magnetic-field-dependent magnetization measurements in fields up to 5 T were made using a superconducting quantum interference device magnetometer, which has a high temperature capability so that the covered temperature-range is $5 \leq T \leq 750$ K. A vibrating sample magnetometer was also used to attain temperatures in the range $300 \leq T \leq 900$ K. To monitor the growth of the ferromagnetic Ni_2MnSb precipitates, powder samples of $x = 5.4$ were annealed at three different temperatures, 650, 700, and 750 K, at four time-scales $10^4, 10^5, 4.5 \times 10^5,$ and 10^6 s (2.8, 28, 125, and 280 h, respectively) at each temperature and were used for the x-ray diffraction (XRD) measurements. XRD measurements were carried out in the angular range $25^\circ \leq 2\theta \leq 100^\circ$ using a Cu $K\alpha$ radiation. The diffractometer (Panalytical) was used in the Bragg-Brentano geometry with the sample placed on a zero-background sample holder which was spun during the measurements. The data were refined using JANA software.²¹

III. RESULTS

A. Magnetization

The results of $M(T)$ measurements for $\text{Ni}_{50}\text{Mn}_{50-x}\text{Sb}_x$ are given in Figs. 1(a)–1(d). The measurements are performed on sequential warming and cooling cycles with the temperature changing at a rate of 4 K min⁻¹ to examine the characteristics of the segregation.

In Fig. 1(a) for $x = 5.4$, the data taken from 300 K to 600 K and back practically retrace. Further warming to 650 K and back to 400 K led to different initial values at 400 K showing that the sample decomposes each time it is brought up to 650 K. When the temperature is further swept up to 700 K,

TABLE I. Compositions of the $\text{Ni}_{50}\text{Mn}_{50-x}\text{Sb}_x$ samples determined by EDX analysis and the valence electron concentrations e/a .

Ni	Mn	Sb	e/a
51.9	42.7	5.4	8.40
50.3	39.6	10.1	8.30
51.5	36.0	12.5	8.25
49.7	35.0	15.3	8.20

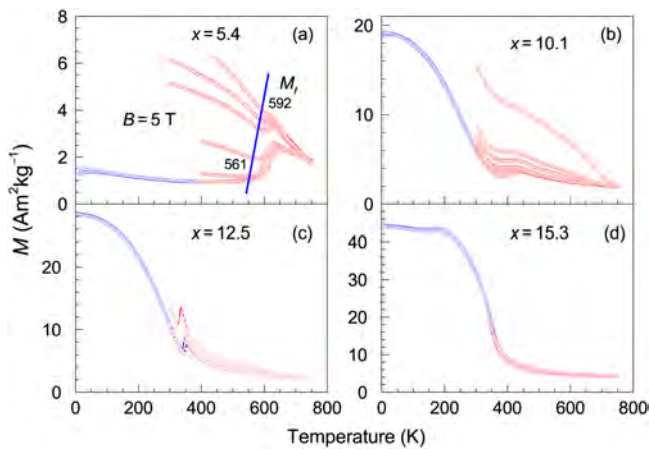


FIG. 1. Checking for decomposition in $\text{Ni}_{50}\text{Mn}_{50-x}\text{Sb}_x$ by sequential warming and cooling $M(T)$ in the range $300 \leq T \leq 750$ K in 5 T. (a) $x = 5.4$, (b) $x = 10.1$, (c) $x = 12.5$, and (d) $x = 15.3$. The shift of M_f to higher temperature as decomposition progresses is distinct for $x = 5.4$ in (a). $M(T)$ measurements in the initial state of the samples for $5 \leq T \leq 300$ K are shown with the blue data.

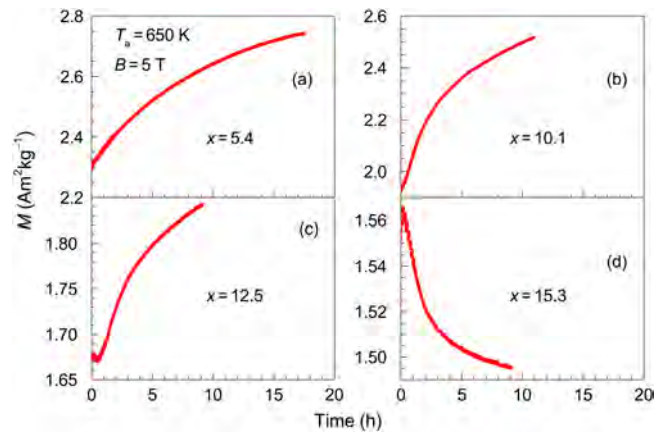


FIG. 2. M -time measurements of $\text{Ni}_{50}\text{Mn}_{50-x}\text{Sb}_x$ samples. Measurements were performed in 5 T magnetic field at $T_a = 750$ K. (a) $x = 5.4$, (b) $x = 10.1$, (c) $x = 12.5$, and (d) $x = 15.3$.

the segregation further develops, and when warmed from 300 K to 750 K, the segregation becomes more obvious. For $T \geq 600$ K, the sample is then in the austenite state.

Similar data for $x = 10.1$ are shown in Fig. 1(b). Although segregation effects are already observed at $T_a = 550$ K, it becomes distinctly clear in the uppermost curve for the sequence $300 \leftrightarrow 750$ K, whereby $M(T)$ exhibits a clear increase at the lower temperature end on decreasing temperature from 750 K. This sample is in the cubic austenite state at 750 K, and the forward and reverse martensitic transitions occur around the peak position.

Sequential $M(T)$ measurements for $x = 12.5$ are shown in Fig. 1(c). Decomposition in the time-scale of these measurements is less significant and only becomes appreciable when the temperature is brought up to 750 K and back down to 300 K (uppermost curve). It becomes more evident at longer time-scales as will be discussed below. The peak in $M(T)$ at about 350 K is due to the martensitic transition. For $M(T)$ of $x = 15.3$, shown in Fig. 1(d), the decomposition becomes insignificant even at 750 K.

Time-dependent magnetization measurements, $M(t)$, for all compositions are given in Figs. 2(a)–2(d). In these measurements, a part of the powder samples was annealed in the magnetometer under 5 T at $T_a = 650$ K for about 10 h (18 h for $x = 5.4$), and the magnetization-change was recorded over time. While $M(t)$ increases with time for $x = 5.4, 10.1$, and 12.5, it decreases for $x = 15.3$. For $x = 5.4, 10.1$, and 12.5, the contribution to the magnetization of the growing ferromagnetically correlated precipitates overweighs the contribution to the magnetization from the initially weakly magnetic samples³⁰ plus that from the growing AF parts so that $M(t)$ increases with increasing time. For $x = 15.3$, the samples are in the austenite state where FM correlations are already strong in the

initial state, so that the generating AF matrix on annealing contributes more dominantly to the magnetization leading to a decrease in $M(t)$ with increasing time.

To check for features that may be masked in the high-field $M(T)$ measurements shown in Fig. 1, we have carried out $M(T)$ measurements in remanence ($B = 0$; the true field due to flux trapping is about 0.5 mT). The results are shown in Fig. 3. The annealed samples (cf. Fig. 2) were measured in remanence first between 10 and 300 K in a decreasing-increasing temperature-sequence. The samples were then removed and inserted into the high-temperature oven and measured between 300 and 600 K in an increasing-decreasing temperature-sequence. In the range $5 \leq T \leq 300$ K, the data retrace for $x = 5.4$ and $x = 10.1$, whereas differences related to intermartensitic transitions and the occurrence of Hopkinson's peaks are found for $x = 12.5$ and $x = 15.3$ close to the martensite and austenite Curie temperatures, T_C^M for $x = 10.1$ and 12.5, and T_C^A for $x = 15.3$, respectively.^{34,35} These are shown with vertical arrows. These Curie temperatures corresponding to those of the non-decomposed parts are in good agreement with earlier measurements on the initial state of the samples.³⁰ During the measurement, which is made at a rate of 4 K min^{-1} , decomposition further progresses at temperatures around 600 K. Since no magnetic-field is applied during the measurement, the further growth of the precipitates occurs with random pinning direction of the shell leading to a lower value in the magnetization. This causes $M(T)$ to run at lower values in the decreasing-temperature branch in the cases for $x = 5.4, 10.1$, and 12.5. For $x = 15.3$, this property is not observed, further confirming that decomposition becomes less significant at this composition. For $x = 10.1$ and 12.5, the Curie temperatures of the precipitates appear as a feature indicated as T_C^{prec} . These correspond to about 330–340 K, which lies in the range of T_C^A of the full Heusler compound $\text{Ni}_{50}\text{Mn}_{25}\text{Sb}_{25}$.³⁰ Therefore, the chemical

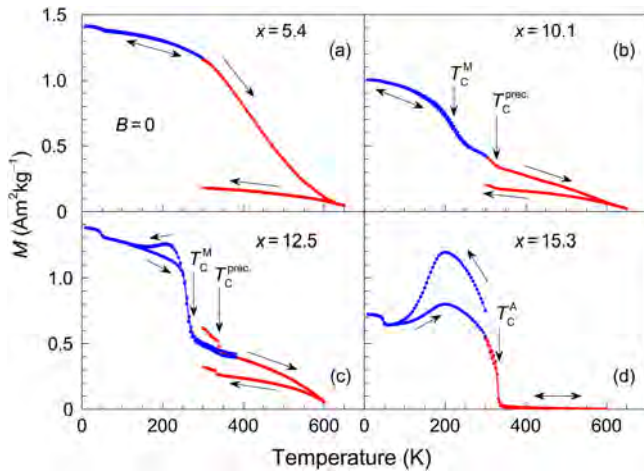


FIG. 3. $M(T)$ measured in remanence of (a) $x = 5.4$, (b) $x = 10.1$, (c) $x = 12.5$, and (d) $x = 15.3$ annealed at 650 K (cf. Fig. 2). Blue data: Measurements for $5 \leq T \leq 300$ K for decreasing-increasing sequence. Red data: Measurements for $300 \leq T \leq 600$ K for increasing-decreasing sequence. Vertical arrows indicate Curie temperatures. Other arrows indicate the temperature-change direction.

composition of the precipitates is expected to be close to this, which would be in agreement with the decomposition reaction given in Eq. (1). It is difficult to assign a T_C^{prec} for the precipitates in the $x = 5.4$ -sample. However, $M(T)$ of this sample also shows a FM-like temperature-dependence unlike its initial state which is AF.³⁰ The decrease in $M(T)$ with increasing temperature becomes faster around the temperature estimated as T_C^{prec} for the samples in Figs. 3(b) and 3(c), so that the precipitates developing in the $x = 5.4$ sample can be expected to have a similar Curie temperature.

We next present in Fig. 4 the results on $M(B)$ for $x = 5.4$ at 400 K obtained on annealing at 600 K. The sample is first brought to 600 K, annealed for 1 h, and $M(B)$ is measured at 400 K [Fig. 4(a)]. The procedure is repeated for a total of 6 h. In Fig. 4(b) we define the difference in the maximum and minimum magnetizations at $B = 0$ as the hub M_h and the vertical shift of the displaced hysteresis as M_{vs} . The exchange-bias and the coercive field, B_{eb} and B_c , are also shown. Since the initial state ($t_a = 0$) is AF, B_{eb} and B_c , as well as H_{eb} and H_c , vanish. For finite t_a , all parameters steadily increase as the amount of precipitates increases as will be presented in Sec. III B.

B. Precipitate size ($x = 5.4$)

Shell-FM precipitation is most distinct at compositions when the Z-element is at around $x = 5$. We carry out XRD experiments to obtain information on the precipitate-size and its evolution with T_a and t_a in a similar manner we had earlier reported for $\text{Ni}_{50}\text{Mn}_{45}\text{In}_5$.²⁵ The broadening of the spectral lines in an XRD pattern provides information on strain and grain size. After correcting for the instrumental broadening,

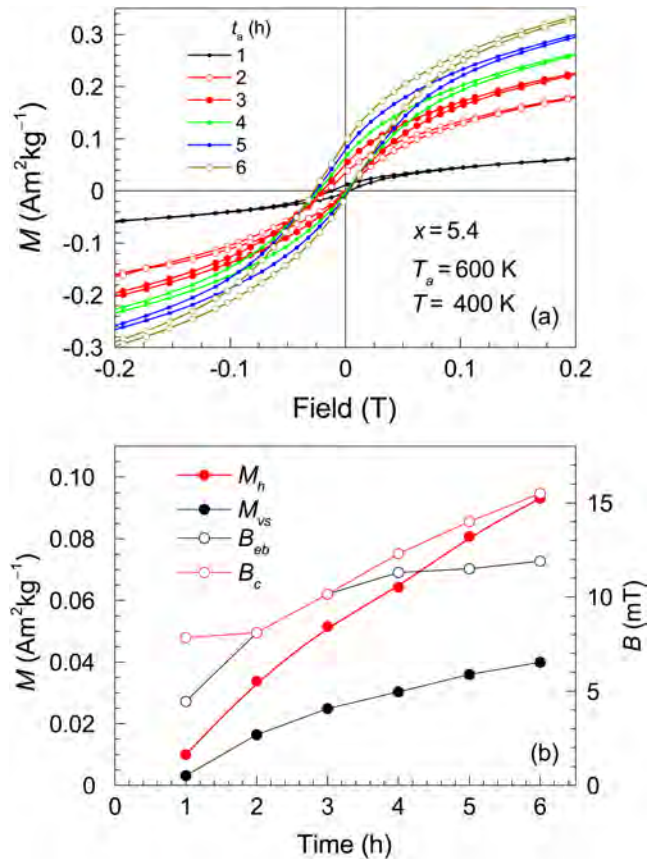


FIG. 4. $M(H)$ and characteristic field and magnetization parameters for $x = 5.4$. (a) $M(H)$ at 400 K obtained after annealing at 600 K for various sequential annealing times. (b) The characteristic magnetization parameters, M_h and M_{vs} , and the characteristic field parameters, H_{eb} and H_c .

the precipitate-size can be estimated from

$$D_{hkl} = \frac{k\lambda}{(\text{FWHM}) \cos(\theta)_{hkl}}, \quad (2)$$

where D_{hkl} is the precipitate diameter, h, k, l are Miller indices, the factor k is taken as 0.89, FWHM is the full-width-at-half-maximum corrected for the instrumental broadening and strain, and $(\theta)_{hkl}$ is the peak-angle. FWHM can be expressed as the difference between the measured FWHM, $(\text{FWHM})_{\text{meas}}$, and the contribution from both strain effects and the instrumental resolution $(\text{FWHM})_{\text{strain+ires}}$ so that

$$(\text{FWHM}) = (\text{FWHM})_{\text{meas}} - (\text{FWHM})_{\text{strain+ires}}; \quad (3)$$

from here, D_{hkl} can be estimated by substituting Eq. (3) in Eq. (2).

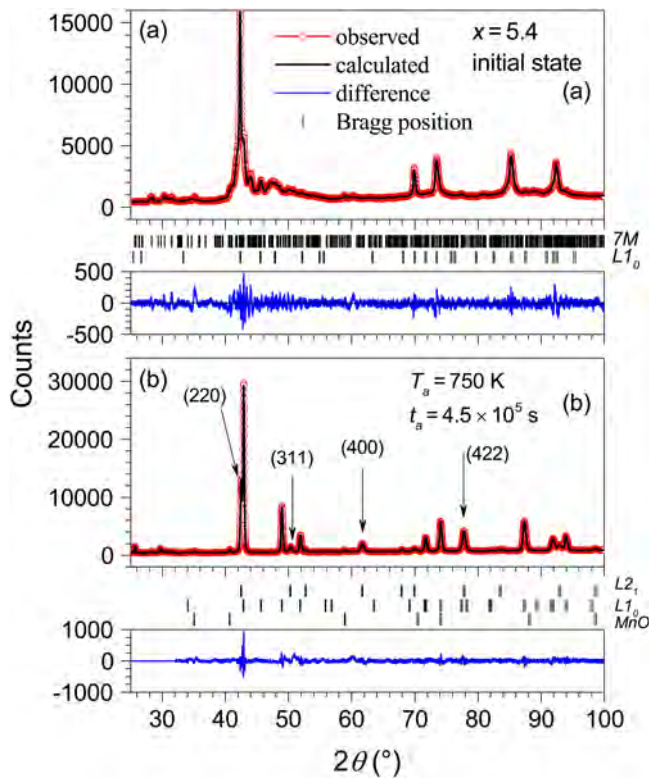


FIG. 5. Room-temperature XRD measurements showing the evolution of the initial $7M+L_{10}$ structure (a) into the L_{10} and cubic Heusler structure (b) at $T_a = 750$ K. The observed, calculated, and difference spectra, as well as the Bragg positions, are given in the figures. The peaks related to the cubic structure are indexed in part (b).

When the sample $x = 5.4$ is annealed at temperatures $650 \leq T_a \leq 750$ K, it decomposes, and cubic precipitates of $Ni_{50}Mn_{25}Sb_{25}$ are formed. As decomposition progresses, peaks related to the cubic structure first appear and become more distinct. We show first the difference in the XRD patterns of the initial state in Fig. 5(a) and the state after the sample is annealed at 750 K for 4.5×10^5 s (125 h) in Fig. 5(b). Le Bail treatments of the spectra show that the structure of the initial state is mixed, modulated $7M$, and non-modulated L_{10} martensite in agreement with earlier measurements. In the annealed state, the $7M$ structure is no longer observed and only peaks related to the L_{10} martensite structure remain, while peaks related to the cubic Heusler phase begin to appear. Also, peaks related to trace amounts of MnO become apparent in the annealed case in Fig. 5(b).

Secondly, we show the time-evolution of the decomposition at 750 K in the XRD patterns in Fig. 6. The evolution of the $7M$ martensite structure into the L_{10} structure and the concurrent emergence of the cubic Heusler peaks indexed in the diagram are distinctly observed. These become sharper

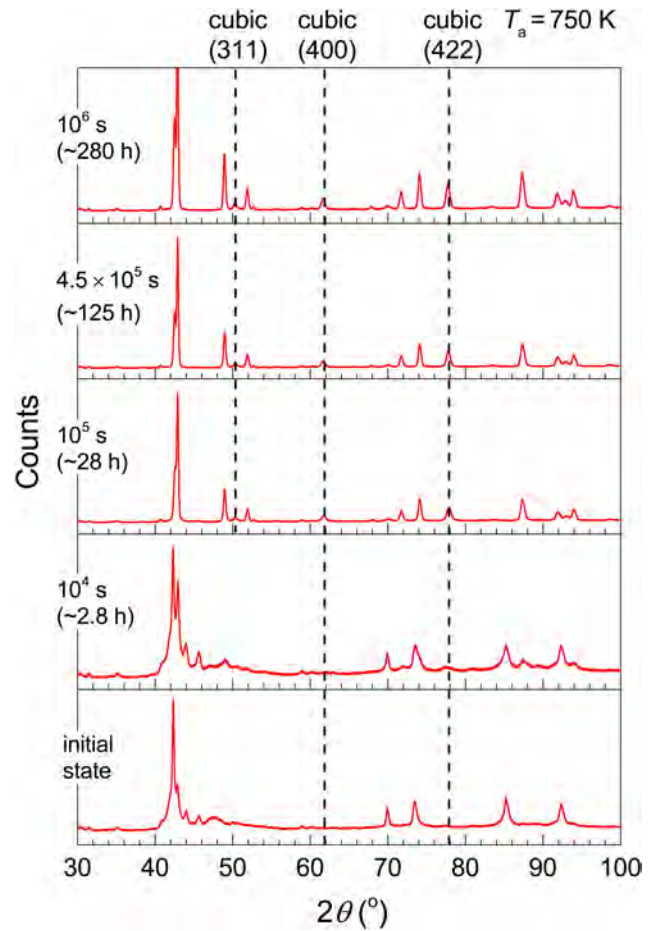


FIG. 6. The evolution of the (311), (400), and (422) peaks for $T_a = 750$ K and for various t_a 's.

for longer t_a . From similar data obtained at various T_a , we have obtained using (2) the results on the t_a -dependence of D for the (311), (400), and (422) peaks shown in Fig. 7. For $T_a = 650$ K, a reasonable estimation for the precipitate-size can only be made for $t_a = 280$ h since the time-evolution of the peak-intensities is too weak for shorter t_a . For this t_a , the size is about 5–10 nm. Scherrer analysis for the (311) and (422) peaks [Figs. 7(a) and 7(c)] yields similar behaviors in D vs. t_a with D -values reaching at $t_a = 280$ h to about 10 nm for $T_a = 650$ K, 15–20 nm for $T_a = 700$ K, and 40–50 nm for $T_a = 750$ K. An analysis of the (400) peak, on the other hand, gives smaller values with 5 nm for $T_a = 650$ K, 10 nm for $T_a = 700$ K, and about 20 nm for $T_a = 750$ K. The (311) occurs at an angle where other close-lying peaks related to the L_{10} phase are found, and the (422) peak is at higher angles which reduces the reliability of the Scherrer analysis. Actually, the (400) peak is the most isolated and could represent better the t_a -dependence of D . In fact, the values obtained from the

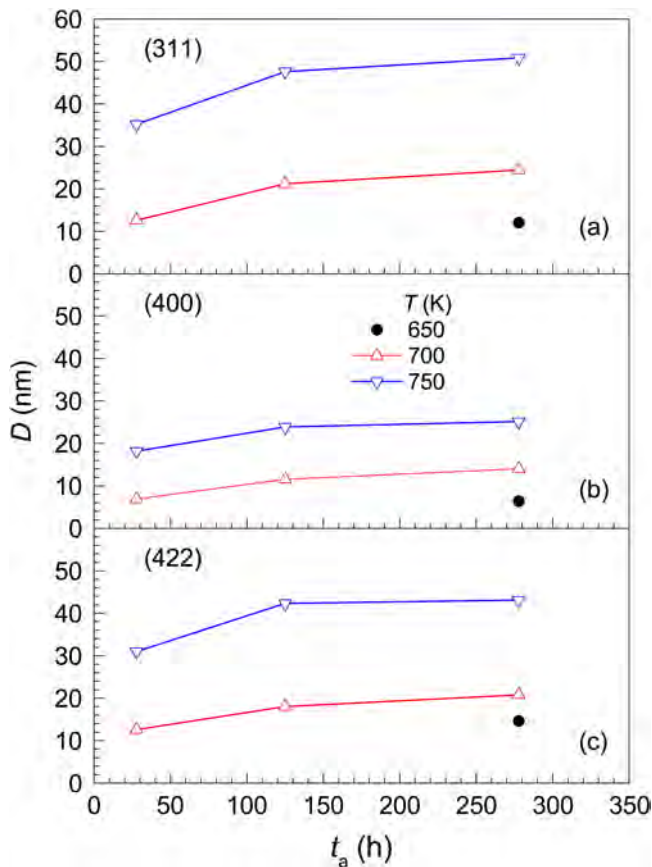


FIG. 7. t_a -dependence of the precipitate size determined from the Scherrer analysis of the cubic peaks (a) (311), (b) (400), and (c) (422).

(400) peak are in better agreement with a similar analysis performed for $\text{Ni}_{50}\text{Mn}_{45}\text{In}_5$.²⁵

We have also measured $M(T)$ in 5 T and up to 900 K of the samples with $x = 5.4$ decomposed at 750 K for various annealing times in $B = 0$ to observe further changes in the position of the martensitic transition temperatures. The results are shown in Fig. 8. In Fig. 8(a), $M(T)$ crosses the austenite-finish temperature at $A_f \approx 720$ K, showing that the characteristic martensitic transition temperatures for $t_a = 10^4$ s have moved further up with respect to those shown in Fig. 1(a). At temperatures around 900 K, the decomposed samples reset to their initial state. Therefore, on decreasing temperature, $M(T)$ follows a different path below about 800 K because decomposition begins to take place once again when the reset-sample is slowly cooled at a rate of 4 Kmin^{-1} during the measurements. Around 800 K, $M(T)$ begins to increase with decreasing temperature, since now the decomposition is taking place in a magnetic field providing a preferred orientation for the developing shell-FM spins. The martensite-start temperature M_s is now at about 670 K. Figures 8(b)–8(d) show similar behavior among themselves, however, somewhat

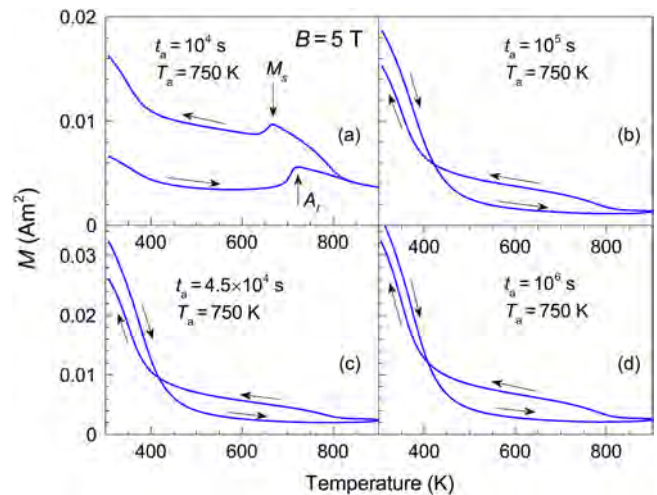


FIG. 8. $M(T)$ measurements in 5 T for the samples annealed at 750 K and $B = 0$ for (a) 10^4 s, (b) 10^5 s, (c) 4.5×10^5 s, and (d) 10^6 s.

different than in Fig. 8(a). For these cases, the length of t_a appears to shift the transition temperatures to well above the measured temperature range. On decreasing temperature, decomposition again begins to occur below 880 K so that $M(T)$ increases with decreasing temperature and higher values down to 500 K, since the decomposition progresses in 5 T down to about 550 K.

IV. DISCUSSION

Shell-FM precipitates are found in all decomposed $\text{Ni}_{50}\text{Mn}_{45}\text{Z}_5$ systems. What is distinct about $\text{Ni}_{50}\text{Mn}_{45}\text{Sb}_5$ is that the decomposition temperature of 650 K lies within the austenite state and not within the martensite state as for the other Z-elements. The martensitic transition lies at lower temperatures making it possible to observe a change in the martensitic transition temperature as decomposition progresses. As seen in Fig. 1, the martensite finish temperature shifts to higher values with progressing decomposition. The difference in the transition temperature between the initial state (561 K) and the last $M(T)$ run (592 K) amounts to about 30 K which corresponds to a valence electron concentration difference of $0.1 e/a$; namely, in this case, an enrichment in Mn of about 0.2 at. % within the time the sample spends in the range $550 \leq T_a \leq 750$ K. The decomposition in these time scales is only partial and to achieve a full decomposition at $T_a = 650$ K requires periods of up to about a year. The progressive increase of M_s indicates that the matrix composition changes gradually toward NiMn as Sb is consumed from the surroundings by the emerging $\text{Ni}_{50}\text{Mn}_{25}\text{Sb}_{25}$ Heusler precipitate. For longer annealing times, the characteristic martensitic transition temperatures move up to distinctly higher temperatures as seen in Fig. 8(a) and eventually move to temperatures beyond the reset-temperature of about 900 K [Figs. 8(b)–8(d)].

The time-dependence of the magnetization, reflecting the time-evolution of the decomposition, features an increase or a decrease at different rates. For $x = 5.4$ and 10.1 , the change in M at 650 K between the starting time and 10 h is about the same and increases over time. For $x = 12.5$, the increase-rate decreases over the same period, and for $x = 15.3$, we observe a decrease in M over time. The rate of change of M with time depends on the balance of the emerging FM and the strengthening of AF exchange as the matrix becomes more Mn-rich so that various scenarios can be encountered. The sample $x = 5.4$ is AF and $x = 10.1$ is weakly FM. At these concentrations, the magnetization of the growing FM parts overwhelms the smaller magnetization of the AF parts. As the Sb concentration increases, FM interactions become stronger so that the magnetization of any newly emerging FM component starts becoming masked by the growing AF component. Thus, the rate of increase of the magnetization becomes smaller as for $x = 12.5$ and eventually reverses as the strength of the growing AF component becomes more dominant, as for $x = 15.3$.

The remanent magnetization can reveal features that become masked when the magnetization is measured in high fields (Fig. 1). High-fields can magnify the magnetization so that a small difference in the magnetic moment between the austenite and martensite phases can be revealed, as is the case in Fig. 1. However, high-fields can also wash out features related to the magnetic ordering temperatures and any other features related to magnetic frustration and magnetic pinning effects. Figure 3 reveals further features related to magnetic ordering due to the decomposition process. For $x = 5.4$, the decrease in $M(T)$ with increasing temperature is due to increase in the fluctuations of the pinned shell-spins and the disordering of the $\text{Ni}_{50}\text{Mn}_{25}\text{Sb}_{25}$ core, which have $T_C \sim 330\text{--}340$ K. This is slightly higher than T_C^{prec} observed for $\text{Ni}_{50}\text{Mn}_{45}\text{In}_5$, which is around 320 K due to the fact that T_C^A for Z as Sb is, in general, higher than for Z as in Ref. 30. The shell-FM fluctuations persist up to the annealing temperature. A similar case is observed for $x = 10.1$ and 12.5 .

The shell-FM pinning appears to have somewhat different properties than the case in $\text{Ni}_{50}\text{Mn}_{50-x}\text{Z}_x$, where Z is a main group element other than Sb. Both vertical and horizontal shifts in $M(B)$ occur in $\text{Ni}_{50}\text{Mn}_{45}\text{Sb}_5$ [Fig. 4(a)], whereas only vertical shifts have been found for the cases Z as Al, Ga, In, and, Sn.^{22,23,36,37} An exchange-bias effect at temperatures as high as $400\text{--}500$ K is not usual. However, it can be plausible due to the strong exchange coupling at the interface of the precipitate and the surrounding AF-NiMn where both the AF surrounding and the FM shell are long-range ordered. However, to answer why this occurs in the case when Z is Sb requires further investigations.

The Scherrer analysis provides an estimate of the average size and provides no information on the actual size distribution. Microscopy studies would provide better information on the size distribution. Nevertheless, we can observe here a systematic increase of the size of the precipitates with increasing T_a and increasing t_a . For $T_a = 650$ K, an analysis cannot be performed from the data obtained for the shorter periods,

since the peaks related to the cubic structure do not stand out. For $T_a = 700$ and 750 K, the decomposition progresses faster, and the peaks are more distinct. The size of the precipitates ranges up to $5\text{--}10$ nm when annealed at 650 K for 180 h and fall in the same range for precipitates in $\text{Ni}_{50}\text{Mn}_{45}\text{In}_5$ reported earlier.²⁵

V. CONCLUSION

We have studied the decomposition of a series of Mn-rich $\text{Ni}_{50}\text{Mn}_{50-x}\text{Sb}_x$ compounds. The decomposition leads to the shell-FM effect for $x = 5.4$ persisting up to $x = 15.3$, at which it becomes less significant. Both vertical and horizontally shifted $M(B)$ curves are obtained typical for the occurrence of the shell-FM effect. This composition also corresponds to the range in which functionalities related to magnetostructural transitions are found. Therefore, it is important to understand the metallurgical state of the sample arising from heat-treatments to be able to be conclusive about functional properties. The Scherrer analysis performed for XRD patterns obtained for in $\text{Ni}_{50}\text{Mn}_{45}\text{Sb}_5$ yields a precipitate-size of about $5\text{--}10$ nm.

Next to the vertical shift of the hysteresis loop, a further exchange-bias effect is observed in $\text{Ni}_{50}\text{Mn}_{50-x}\text{Sb}_x$ at temperatures as high as $400\text{--}500$ K. The origin of this effect is presently not known and requires further studies. This is also required to verify the size and the size distribution of the shell-FM precipitates with microscopy and small angle x-ray and neutron scattering techniques.

ACKNOWLEDGMENTS

This work was supported by the Deutsche Forschungsgemeinschaft (DFG) (No. SPP 1599). The DAAD is gratefully acknowledged.

REFERENCES

- 1A. Planes, L. Mañosa, and M. Acet, *J. Phys. Condens. Matter* **21**, 233201 (2009).
- 2O. Söderberg, A. Sozinov, Y. Ge, S. P. Hannula, and V. K. Lindroos, in *Handbook of Magnetic Materials* (Elsevier, 2006), Vol. 16, pp. 1–39.
- 3R. Kainuma, Y. Imano, W. Ito, Y. Imano, W. Ito, Y. Sutou, H. Morito, S. Okamoto, O. Kitakami, K. Oikawa, A. Fujita, T. Kanomata, and K. Ishida, *Nature* **439**, 957 (2006).
- 4V. Franco, J. S. Blázquez, B. Ingale, and A. Conde, *Annu. Rev. Mater. Res.* **42**, 305 (2012).
- 5J. Liu, T. Gottschall, K. P. Skokov, J. D. Moore, and O. Gutfleisch, *Nat. Mater.* **11**, 620 (2012).
- 6S. Chatterjee, S. Giri, S. Majumdar, and S. K. De, *J. Phys. D Appl. Phys.* **42**, 065001 (2009).
- 7S. Kaufmann, U. K. Rößler, O. Heczko, M. Wuttig, J. Buschbeck, L. Schultz, and S. Fähler, *Phys. Rev. Lett.* **104**, 145702 (2010).
- 8V. K. Sharma, M. K. Chattopadhyay, and S. B. Roy, *Phys. Rev. B* **76**, 140401(R) (2007).
- 9R. Y. Umetsu, X. Xu, W. Ito, T. Kihara, K. Takahashi, M. Tokunaga, and R. Kainuma, *Metals* **4**, 609 (2014).
- 10B. M. Wang, Y. Liu, P. Ren, B. Xia, K. B. Ruan, J. B. Yi, J. Ding, X. G. Li, and L. Wang, *Phys. Rev. Lett.* **106**, 077203 (2011).
- 11Z. D. Han, B. Qian, D. H. Wang, P. Zhang, X. F. Jiang, C. L. Zhang, and Y. W. Du, *Appl. Phys. Lett.* **103**, 172403 (2013).
- 12A. Çakır, M. Acet, and M. Farle, *Phys. Rev. B* **93**, 094411 (2016).

- ¹³A. Çakır, M. Acet, and M. Farle, *Sci. Rep.* **6**, 28931 (2016).
- ¹⁴D. L. Schlager, R. W. McCallum, and T. A. Lograsso, *J. Alloys Compd.* **463**, 38 (2008).
- ¹⁵W. M. Yuhasz, D. L. Schlager, Q. Xing, K. W. Dennis, R. W. McCallum, and T. A. Lograsso, *J. Appl. Phys.* **105**, 07A921 (2009).
- ¹⁶W. M. Yuhasz, D. L. Schlager, Q. Xing, R. W. McCallum, and T. A. Lograsso, *J. Alloys Compd.* **492**, 681 (2010).
- ¹⁷K. Niitsu, K. Minakuchi, X. Xu, M. Nagasako, I. Ohnuma, T. Tanigaki, Y. Murakami, D. Shindo, and R. Kainuma, *Acta Mater.* **122**, 166 (2017).
- ¹⁸C. Felser, L. Wollmann, S. Chadov, G. H. Fecher, and S. S. P. Parkin, *APL Mater.* **3**, 041518 (2015).
- ¹⁹A. Çakır, see <https://www.youtube.com/watch?v=0VlSksW2G-s> for shell ferromagnetism.
- ²⁰A. Çakır, see <https://www.youtube.com/watch?v=v4OiTxPnSkY> for perpendicular anisotropy of a shell ferromagnet.
- ²¹V. Petricek, M. Dusek, and L. Palatinus, *Z. Kristallogr.* **229**(5), 345 (2014).
- ²²A. Çakır, M. Acet, U. Wiedwald, T. Krenke, and M. Farle, *Acta Mater.* **127**, 117 (2017).
- ²³T. Krenke, A. Çakır, F. Scheibel, M. Acet, and M. Farle, *J. Appl. Phys.* **120**, 243904 (2016).
- ²⁴F. Scheibel, D. Spoddig, R. Meckenstock, A. Çakır, M. Farle, and M. Acet, *AIP Adv.* **7**, 056425 (2017).
- ²⁵L. Dincklage, F. Scheibel, A. Çakır, M. Farle, and M. Acet, *AIP Adv.* **8**, 025012 (2018).
- ²⁶M. Khan, I. Dubenko, S. Stadler, and N. Ali, *Appl. Phys. Lett.* **91**, 072510 (2007).
- ²⁷M. Khan, N. Ali, and S. Stadler, *J. Appl. Phys.* **101**, 053919 (2007).
- ²⁸M. Khan, I. Dubenko, S. Stadler, and N. Ali, *J. Phys. Condens. Matter* **20**, 235204 (2008).
- ²⁹S. Chatterjee, S. Giri, S. Majumdar, and S. K. De, *J. Magn. Magn. Mater.* **320**, 617 (2008).
- ³⁰S. Aksoy, M. Acet, E. F. Wassermann, T. Krenke, X. Moya, L. Mañosa, A. Planes, and P. P. Deen, *Phil. Mag.* **89**, 1 (2004).
- ³¹I. Dubenko, M. Khan, A. K. Pathak, B. R. Gautam, S. Stadler, and N. Ali, *J. Magn. Magn. Mater.* **321**, 754 (2009).
- ³²R. Sahoo, A. K. Nayak, K. G. Suresh, and A. K. Nigam, *J. Magn. Magn. Mater.* **324**, 1267 (2012).
- ³³R. Zhang, M. Qian, X. Zhang, F. Qin, L. Wei, D. Xing, X. Cui, J. Sun, L. Geng, and H. Peng, *J. Magn. Magn. Mater.* **428**, 464 (2017).
- ³⁴J. Hopkinson, *Philos. Trans. R. Soc. Lond. A* **180**, 443 (1889).
- ³⁵A. Çakır, L. Righi, F. Albertini, M. Acet, M. Farle, and S. Aktürk, *J. Appl. Phys.* **114**, 183912 (2013).
- ³⁶A. Çakır and M. Acet, *J. Magn. Magn. Mater.* **448**, 13 (2018).
- ³⁷A. Çakır and M. Acet, *AIP Adv.* **7**, 056424 (2017).